ACS APPLIED ENERGY MATERIALS

Forum Article

www.acsaem.org

Influence of the Ligand Stripping on the Transport Properties of Nanoparticle-Based PbSe Nanomaterials

Doris Cadavid,*[,†] Silvia Ortega,[‡] Sergio Illera,[§] Yu Liu,[∥] Maria Ibáñez,[∥] Alexey Shavel,[‡] Yu Zhang,[‡] Mengyao Li,[‡] Antonio M. López,[⊥] Germán Noriega,[#] Oscar Juan Durá,[▽] M. A. López de la Torre,[▽] Joan Daniel Prades,[§] and Andreu Cabot*[,‡,%]

[†]Departamento de Física, Universidad Nacional de Colombia, Ciudad Universitaria, 111321, Bogotá, Colombia

[‡]Catalonia Institute for Energy Research - IREC, 08930 Sant Adrià de Besòs, Barcelona, Spain

[§]Departament d'Electrònica, Universitat de Barcelona, C. Martí i Franquès 1, 08028 Barcelona, Spain

[∥]Institute of Science and Technology Austria, Am Campus 1, 3400 Klosterneuburg, Austria

[⊥]Departament d'Enginyeria Electrònica, Universitat Politècnica de Catalunya, EPSEVG, 08800 Vilanova i la Geltrú, Barcelona, Spain

[#]Cidete Ingenieros S.L., Anselm Clavé 98, 08800 Vilanova i la Geltrú, Barcelona, Spain

[▽]Departamento de Física Aplicada, Universidad de Castilla-La Mancha, Avd. Camilo José Cela, Edificio Politécnico, ETSII, 13071 Ciudad Real, Spain

[%]ICREA, Pg. Lluís Companys 23, 08010 Barcelona, Spain

Supporting Information

ABSTRACT: Nanomaterials produced from the bottom-up assembly of nanocrystals may incorporate ~10^{20}−10^{21} cm^{-3} not fully coordinated surface atoms, i.e., ~10^{20}−10^{21} cm^{-3} potential donor or acceptor states that can strongly affect transport properties. Therefore, to exploit the full potential of nanocrystal building blocks to produce functional nanomaterials and thin films, a proper control of their surface chemistry is required. Here, we analyze how the ligand stripping procedure influences the charge and heat transport properties of sintered PbSe nanomaterials produced from the bottom-up assembly of colloidal PbSe nanocrystals. First, we show that the removal of the native organic ligands by thermal decomposition in an inert atmosphere leaves relatively large amounts of carbon at the crystal interfaces. This carbon blocks crystal growth during consolidation and at the same time hampers charge and heat transport through the final nanomaterial. Second, we demonstrate that, by stripping ligands from the nanocrystal surface before consolidation, nanomaterials with larger crystal domains, lower porosity, and higher charge carrier concentrations are obtained, thus resulting in nanomaterials with higher electrical and thermal conductivities. In addition, the ligand displacement leaves the nanocrystal surface unprotected, facilitating oxidation and chalcogen evaporation. The influence of the ligand displacement on the nanomaterial charge transport properties is rationalized here using a two-band model based on the standard Boltzmann transport equation with the relaxation time approximation. Finally, we present an application of the produced functional nanomaterials by modeling, fabricating, and testing a simple PbSe-based thermoelectric device with a ring geometry.

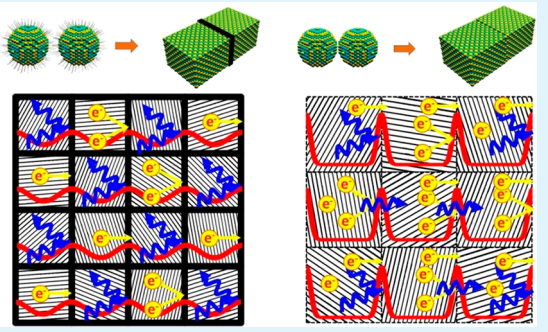

KEYWORDS: *nanoparticle, colloid, chalcogenide, thermoelectricity, ligand displacement, transport properties*

1. INTRODUCTION

The use of colloidal nanocrystals (NCs) with tuned size, shape, crystal phase, and composition as building blocks to engineer nanomaterials provides unmatched control over material parameters at the nanometer scale and a huge design flexibility to optimize their functional properties.[1−3] At the same time, bottom-up solution-processing technologies enable the production of functional materials by design in a cost-effective manner. These bottom-up solution-processing technologies are particularly well suited to produce thermoelectric (TE) materials and devices, which benefits from nanocrystalline materials to minimize thermal conductivity.[4−11]

Nevertheless, to exploit the full potential of NC-based bottom-up technologies to produce functional nanomaterials, some limitations need to be overcome. The first limitation is the presence of the electrically insulating organic surfactants used to

Special Issue: Thermoelectrics

Received: October 31, 2019
Accepted: December 23, 2019

DOI: 10.1021/acsaem.9b02137
ACS Appl. Energy Mater. XXXX, XXX, XXX−XXX

control NC growth, e.g., long chain alkanes and alkenes with functional groups such as carboxylic and phosphonic acids, thiols, or amines. These surface organic ligands block charge transport, injection, and extraction among NCs and between NCs and the media, thus constraining the performance of bottom-up engineered nanomaterials in all fields where charge transport is involved, e.g., electronics, optoelectronics, catalysis, or thermoelectricity. To remove surface organic ligands, several displacement and exchange procedures, based on the use of substituting shorter-surface species, have been proposed: pyridine,[12] hydrazine-based metal chalcogenide complexes,[13−17] nitrosonium, diazonium,[18] and trialkyl oxonium tetrafluoroborates,[19] tetrafluoroborate acids (HBF_4, HPF_6),[20] tetrabutylammonium iodide, 1,2-ethanedithiol,[21,22] ammonium thiocianate (NH_4SCN),[23,24] Na_2S, NH_4S, K_2Te, K_2S,[20,24−28] or halide anions like Cl^-, Br^-, and I^-,[29−32] among others.[19,33−37]

A second limitation is the tuning of the charge carrier concentration of nanomaterials obtained from the bottom-up assembly of colloidal NCs. The introduction of controlled amounts of external elements within the NC lattice, which is the usual strategy used to dope conventional bulk or thin film semiconductors, is still challenging for some compounds in NC form.[38−43] Another important limitation in this direction is the control of the NC surface composition. Interfaces strongly affect the electronic transport of nanomaterials through two main mechanisms: (i) charge carrier scattering at the potential barriers created in the grain-boundaries affects the charge carrier mobility,[44] and (ii) acceptor and donor states associated with non-fully coordinated ions or impurities at the interfaces affect the charge carrier concentration.[45] Even stoichiometric and pure nanomaterials obtained from the bottom-up assembly of 10 nm NCs may incorporate 10^{20}−10^{21} cm^{-3} interface atoms not fully coordinated, thus introducing the same amount of potential donor or acceptor states. This large density of interface states may translate into very large charge carrier concentrations and charge transport barriers at crystal interfaces that strongly influence charge transport in the nanomaterial.

Overcoming the two aforementioned limitations is a topic of major interest for the scientific community involved in the development of NC-based bottom-up technologies to produce thin film, nanomaterial, and NC-based devices, such as quantum dot solar cells, catalysts, or thermoelectrics. Nevertheless, most of the works in this direction have focused on the study of ligand exchange strategies to passivate or even introduce controlled amounts of dopants in nonsintered nanoparticle arrays. In spite of the extraordinary progress in this direction, nanomaterials obtained by this strategy still suffer from low charge carrier mobilities and relatively poor performances compared with competing technologies.

In this work, we investigated the effect of the ligand displacement (LD) procedure on the transport properties of consolidated nanomaterials obtained by bottom-up strategies. The influence of the ligand exchange procedure on the nanomaterial transport properties is discussed in the framework of a charge transport model based on the standard Boltzmann transport equation[46] with the relaxation time approximation and developed to fit our experimental data. We used PbSe as the model material owing to its easy synthesis with exceptional size and shape control at the gram scale and its excellent TE properties. In this direction, several metal chalcogenides, and particularly bismuth and lead chalcogenides,[4,7,47] produced using a plethora of synthetic routes, including hydrothermal,[48] solvothermal,[49,50] sonochemical,[51,52] and sol−gel,[53] among others,[54−56] have been demonstrated to display excellent TE properties. Among them, while PbSe has attracted less attention than PbTe- and Bi_2Te_3-based alloys, heavily doped PbSe has been predicted to reach TE figures of merit, ZT up to 2,[57] and experimental ZT values up to 1.6 and 1.5 have been reported for $Pb_{1-x}Na_xSe$ + CdS at 900 K and $Pb_{0.95}Sb_{0.033}Se_{1-y}Te$ at 823 K, respectively.[58,59] Besides, PbSeTe alloys codoped with Na and Cu and alloys of PbSe with $NaSbSe_2$ have reached TE figures of merit ZT up to 1.5 at 860 K[60] and 1.4 near 900 K,[61] respectively.

Beyond studying the influence of the ligand exchange procedure on the TE properties of bottom-up engineered nanomaterials, taking advantage of the versatility of solution-processing technologies, we developed a TE generator with a ring-shape geometry. While current commercial TE devices show the conventional planar architecture and cannot adapt to the huge variety of heat source/sink geometries to optimize thermal energy transfer, solution-processed TE devices can be fabricated with potentially any shape and size. This is here demonstrated by fabricating and testing a simple TE generator with a ring geometry, which can be better adapted to exhaust pipes and similar thermal sources.

2. EXPERIMENTAL SECTION

Materials. Selenium pieces (99.999%), lead acetate trihydrate (99.9%), lead nitrate (99.0%), 1-octadecene (ODE, technical grade 90%), oleic acid (OAc, technical grade 90%), sodium amide (95%), ammonium nitrate (98%), anhydrous methanol, anhydrous chloroform, formamide (FA >99.5%), and dimethylformamide (DMF 99.8%) were purchased from Aldrich. Triocthiylphosphine (TOP, 97%) was purchased from Strem Chemicals. Analytical grade ethanol, hexane, and chloroform were purchased from Panreac. All chemicals were used without further purification. A stock solution of TOPSe (1 M) was prepared dissolving 7.89 g of selenium pieces in 100 mL of TOP. All NC preparations were carried out using standard airless techniques: a vacuum/dry Ar Schlenk line was used for the synthesis and an Ar-filled glovebox for storing and handling oxygen- and moisture-sensitive chemicals.

PbSe NCs. A modified approach to the one developed by J. J. Urban et al.[62] was used to synthesize PbSe NCs. In a typical procedure, 7 mmol (2.8 g) of lead acetate trihydrate and 23 mmol (6.6 g) of OAc were dissolved in 50 mL of ODE. The mixture was heated up to 130 °C under a vacuum for 1.5 h. Afterward, the solution was flushed with Ar and heated up to 190 °C. At this temperature, 12 mL of the TOPSe stock solution was quickly injected. After injection, the reaction temperature was maintained between 180 and 190 °C for 10 min. Then, the solution was cooled using a water bath. PbSe NCs were precipitated and redispersed several times using ethanol and hexane. Finally, PbSe NCs were dispersed in chloroform and stored in the glovebox.

Organic Ligand Replacement. Several salts were used to displace organic ligands from the PbSe NC surface. In a typical procedure and using $NaNH_2$ as an example, PbSe NCs (250 mg) were dispersed in 10 mL of chloroform and mixed at room temperature with 5 mL of $NaNH_2$ solution (0.01 M) in methanol. The solution was shaken for 1−2 min to displace the organic ligands attached to the NC surface. Afterward, NCs were precipitated by centrifugation and thoroughly purified using chloroform/methanol to remove the remaining organic species. Finally, PbSe NCs were precipitated and dried under a vacuum or redispersed in polar solvents like FA, DMF, or ethanol for further analysis. To avoid the oxidation of the chalcogenide NCs, the OL replacement was conducted inside the Ar-filled glovebox.

PbSe Nanomaterial. To produce PbSe bulk nanostructured materials, NCs were dried under a vacuum, annealed at 450 °C for 1 h, and compacted at 350 °C for 2 min into disk-shaped pellets of 10 mm diameter and 1 mm thickness under 40 MPa of pressure. For pellet preparation, we used graphite dies and a custom-made hot press

DOI: 10.1021/acsaem.9b02137
ACS Appl. Energy Mater. XXXX, XXX, XXX−XXX

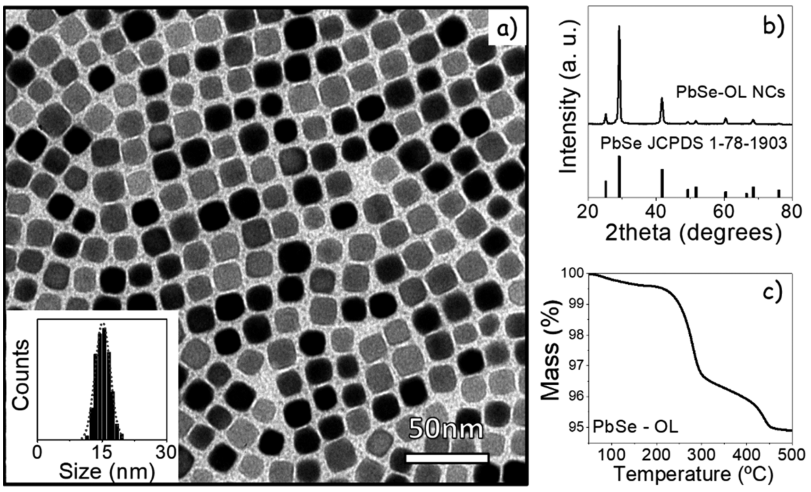

Figure 1. TEM micrograph (a) and histogram of the particle size distribution (a, inset); XRD pattern (b) and TGA profile (c) of 16 ± 2 nm cube-shaped PbSe-OL NCs.

consisting of an induction heater coupled to a hydraulic press kept inside the Ar-filled glovebox.

Ring Thermoelectric Generator. TE rings (39 and 28 mm, outer and inner diameter, respectively, 2 mm thick) were built by filling two Cu concentric rings with dried PbSe NCs followed by uniaxial hot press at 350 °C and 20 MPa for 5 min. Rings were pressed using a custom-made die in the hot press system previously described.

Structural and Chemical Characterization. X-ray power diffraction (XRD) analyses were carried out on a Bruker AXS D8 ADVANCE X-ray diffractometer with Cu Kα1 radiation (λ = 1.5406 Å). The size and shape of the NCs were examined by transmission electron microscopy (TEM) using a ZEISS LIBRA 120, operating at 120 keV accelerating voltage. Scanning electron microscopy (SEM) was performed using a ZEISS Auriga microscope with an energy dispersive X-ray spectroscopy (EDX) detector to study the material's composition. Nuclear magnetic resonance (NMR) spectra (^{1}H NMR) were acquired using a Bruker DRX 500 spectrometer equipped with an 11.7 T magnet and an Avance III console. The spectral frequency was set at 125.7 MHz for ^{13}C. ^{13}C NMR spectra were referenced externally to tetramethyl silane ($SiMe_4$). Spectra were acquired on a 2.5 mm MAS probe head using 20 kHz MAS frequency at room temperature. Thermal gravimetric analyses (TGA) were done using PerkinElmer TGA 4000 equipment. The dried PbSe nanopowders were heated up to 500 °C under a nitrogen flow and a heating ramp of 5 °C/min. Fourier-transform infrared (FTIR) spectra were acquired using an Alpha Bruker FTIR spectrometer with the platinum attenuated total reflectance (ATR) single reflection module, and FTIR data were typically averaged over 64 scans.

Thermoelectric Characterization. Seebeck coefficients and electrical resistivities were measured simultaneously using a Linseis - LSR 3 system under a helium atmosphere. The Seebeck coefficient was obtained using a static DC method, and the electrical resistivity was measured by means of a standard four-probe technique in the temperature range from 300 to 600 K. Thermal conductivity data were obtained from flash diffusivity measurements (Linseis LFA 1000) as a function of temperature. The thermal conductivity was calculated as $\kappa = DC_pd$, where D is the thermal diffusivity, C_p is the heat capacity, and d is the density. C_p was approximated by the formula 0.171 + (2.65 × 10^{-5})T, where T is the absolute temperature.[63−65] At $T > T_D$ (where T_D is the Debye temperature), this equation is consistent with the higher C_p values reported for nanostructured materials, as compared with values obtained by the Dulong−Petit approximation.[66] These alterations of C_p values are caused probably by the high surface to volume ratio in nanostructured materials. Room temperature measurements of the Hall charge carrier concentration and mobility were performed in a four-probe configuration using an electromagnet that generated a magnetic field up to 1.2 T. Current was passed through the sample while the field was varied between 0.1 and 1 T in increments of 0.1 T with an inversion of the field to eliminate voltage probe misalignment effects.

Device Test. Ring TE generators were tested in a custom-made test bench. The inner part of the rings was heated using a cylindrical metal block containing a heating cartridge, while the outer part was maintained cold by means of commercial TE modules attached to a large stainless steel plate. Starting from a 10 °C thermal gradient at room temperature, temperature was increased gradually until reaching 250 °C at the hot side, while the cold side was kept at 60 °C, thus generating a maximum temperature gradient of 190 °C. Temperature was monitored with two thermocouples attached to the cold and hot sides of the ring, respectively, and the open circuit voltage generated between the two Cu electrodes was measured using a Keithley 2400 multimeter.

3. RESULTS AND DISCUSSION

PbSe NCs were synthesized by reacting lead acetate with TOPSe at 190 °C. The presence of OAc in the reacting mixture was essential to limit the PbSe NC growth during their synthesis and to colloidally stabilize them. As-produced PbSe NCs, henceforth referred to as PbSe-OL, had an average size of 16 ± 2 nm with an ∼10% size dispersion, cubic shape (Figure 1a) with [100] facets, and face centered cubic crystallographic phase (fcc, JCPDS 1-78-1903, Figure 1b).

A total of 6% of the total mass of the PbSe-OL NCs obtained after purification with three precipitation and redispersion steps was assigned to surface ligands according to TGA (Figure 1c). The solid state ^{13}C NMR spectrum of PbSe-OL NCs after purification displayed the characteristic C═C peak and the COOH band associated with OAc. We therefore concluded OAc to be the only ligand present at the PbSe-OL NC surface. Taking into account the organic amount measured by TG, a ligand surface concentration of ∼1.4 nm^{-2} was estimated.

The presence of organic ligands at the NC surface was anticipated to strongly limit the performance of any NC-based application that involves charge transport/transfer between/from/to NCs, e.g., photovoltaics, electroluminescent light emitting diodes, thermoelectrics, and catalysis.[67−71] To take full advantage of the convenient processability of colloidal NCs, organic ligands can be chemically or thermally removed after their deposition/assembly. For dense nanomaterials and relatively thick films, chemical processes are not effective because they may not reach the full NC surface. Thus, thermal

DOI: 10.1021/acsaem.9b02137
ACS Appl. Energy Mater. XXXX, XXX, XXX−XXX

decomposition becomes the only viable procedure. Alternatively, native organic ligands can be exchanged in solution, before NC deposition/assembly, by smaller organic or inorganic species able to maintain the NCs colloidally stable, but having a minor effect on the nanomaterial transport properties. There are a myriad of potential ligands that may provide the aforementioned conditions, from metal free anionic ligands (OH^-, NH_2^-) that provide electrostatic stabilization of the NCs to metal chalcogenide complexes MCC obtained using hydrazine[33] to short thiols, e.g., 1,2-ethanedithiol EDT, frequently used in the photovoltaics field.[21,22] Among the potential candidates to displace organic ligands from the PbSe-OL NC surface, hydrazine was discarded due to its toxicity and dangerous manipulation, and sulfur-based compounds were not considered due to their potential to sulfurize the selenide NCs. Thus, other alternative inorganic salts were tested.

To test different salts to displace OAc, PbSe-OL NCs dispersed in chloroform were mixed with a 0.01 M solution of the salt in methanol. The resulting mixture was vigorously shaken at room temperature for a few minutes. During this process, OAc was stripped from the PbSe-OL NC surface and the resulting charge-stabilized PbSe NCs moved to the methanol phase. The obtained PbSe NCs, henceforth referred to as PbSe-LD, were thoroughly washed with chloroform to remove the remaining organic species and finally precipitated and dried under a vacuum. All of these processes were carried out inside an Ar-filled glovebox to avoid oxidation. PbSe-LD NCs preserved the shape and size distributions of the original PbSe-OL NCs (Figure S1) and were dispersible in polar solvents like FA, DMF, or alcohols for a limited amount of time.

In order to characterize the efficiency of the ligand displacement, we used FTIR and NMR spectroscopy. The FTIR spectra for PbSe-LD show that the peaks corresponding to organic ligands are barely visible after the LD (Figure S2), indicating a successful treatment. Solid state ^{13}C NMR analysis of the PbSe NCs treated with $NaNH_2$, henceforth referred to as PbSe-$NaNH_2$, showed the OAc fingerprints to vanish after the ligand displacement process (Figure 2). While a previous work

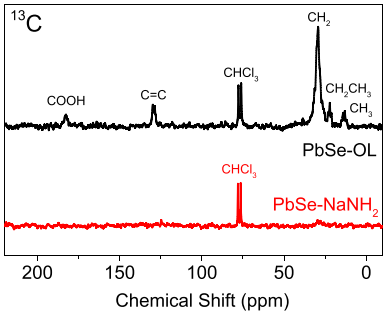

Figure 2. Solid state ^{13}C NMR spectra of PbSe-OL (black) and PbSe-$NaNH_2$ (red) powders dried from a $CHCl_3$ solution. The peaks displayed in the ^{13}C NMR spectra of PbSe-OL are consistent with the OAc fingerprint. The ^{13}C NMR spectra of PbSe-$NaNH_2$ demonstrated the removal of OAc during ligand displacement.

identified NH_2^- as the species remaining at the surface of CdSe NCs,[20] no evidence of NH_2^- fingerprints in the ^1H NMR spectrum of PbSe-$NaNH_2$ NCs could be found. We associated this fact to the facile decomposition of the amide group. It should also be mentioned in this regard that the ligand displacement procedure was carried out in a glovebox, but for NMR characterization, NCs were exposed to air, which may have modified their surface chemistry, especially taking into account the high reactivity of the amide group.

To produce nanostructured PbSe, ~1 g of PbSe NCs was thoroughly cleaned, dried, and annealed at 450 °C for 1 h in argon. The annealed material was afterward compacted at 350 °C under 40 MPa of pressure using a hot press. The relative densities of the final PbSe-OL pellets were around 85%. Those of the PbSe-LD pellets were systematically higher, above 90%. The annealing of PbSe-OL under an inert atmosphere caused the thermal decomposition of the surface OLs. This decomposition left a relatively large amount of carbon, which was quantified by elemental analysis at around 2%. On the other hand, the residual carbon within the final PbSe-LD nanocrystalline powders was within the limit of detection of our system, ~0.1%. EDX and ICP analysis of PbSe-$NaNH_2$ showed no evidence of the presence of Na, pointing out the inefficiency of doping PbSe with Na by this procedure.[63,65,72,73]

During the thermal treatments, the average PbSe-OL crystal size increased from the initial ~16 nm to ~20 nm (Figure 3). The average crystal domain size of the thermal treated PbSe-LD materials was systematically larger. For the PbSe-$NaNH_2$ sample, the crystal size domain increased from 16 to 25−30 nm with the two thermal treatments (Figure 3). These results were confirmed by analyzing the XRD patterns using the Scherrer equation, which showed that the grain size of the compacted material increases up to 1.5 times with respect to the NCs when the NCs were processed without LD. The size increased up to 2.5 times when the NCs were processed after LD (Table S1). We associate the smaller size of the crystal domains obtained from the thermal treatment of PbSe-OL NCs with the creation of a carbon layer that hindered crystal growth.

Figure 4 displays the electrical conductivity (σ), Seebeck coefficient (S), thermal conductivity (κ), power factor (PF), and TE figure of merit (ZT) of consolidated PbSe-OL and PbSe-LD samples. Electrical conductivities of the PbSe-OL samples were relatively low, below 10^4 S m^{-1}. The temperature dependence of the electrical conductivities displayed a step increase in the range from 400 to 500 K. This step was accompanied by a parallel step change of the Seebeck coefficient, which included a sign inversion at around 400 K, from positive to negative values. These step changes and the sign inversion of the Seebeck coefficient suggested the thermal activation of a large concentration of negatively charged carriers above 400 K.

The stripping of the organic ligands before consolidation resulted in a strong increase, up to 2 orders of magnitude, of the electrical conductivity when compared with PbSe-OL samples (Figure 4a). For PbSe-$NaNH_2$, a slight decrease of the electrical conductivity with temperature was observed, consistent with a degenerated semiconductor behavior. Besides, negative Seebeck coefficients with monotonically increasing absolute values were measured for all of the PbSe-LD materials in the entire temperature range tested (Figure 4b). The maximum PF (Figure 4c) was around 1.1 mW m^{-1} K^{-2}. This value was close to the one reported by Ibañez et al., for $PbTe_xSe_yS_{1-x-y}$ nanocomposites with HCl-mediated ligand displacement,[29] but it was higher than the maximum values previously reported for ligand-free PbSe NCs[74] and mixed PbTe/PbSe NCs.[75]

The absolute values of the Seebeck coefficient were lower for PbSe-LD than for PbSe-OL, which denoted higher charge carrier concentrations in the former, in concordance with Hall charge carrier concentrations measured at room temperature: n_H = 2.2 × 10^{19} cm^{-3} for PbSe-LD and n_H = 5 × 10^{15} cm^{-3} for PbSe-OL (Table S2). All of the inorganic ligands tested here resulted

DOI: 10.1021/acsaem.9b02137
ACS Appl. Energy Mater. XXXX, XXX, XXX−XXX

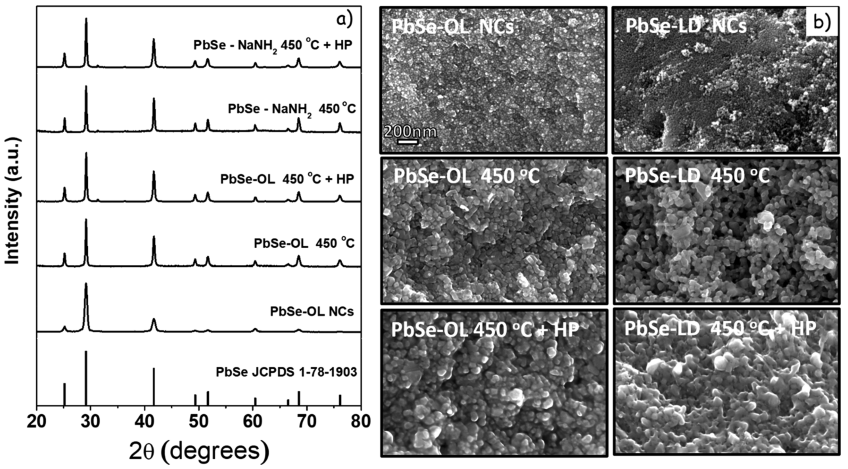

Figure 3. XRD patterns (a) and SEM images (b) of PbSe-OL and PbSe-LD with no thermal treatment (NCs), after heat treatment at 450 °C (450 °C) and after additional hot press at 350 °C and 4 MPa for 2 min (450 °C + HP).

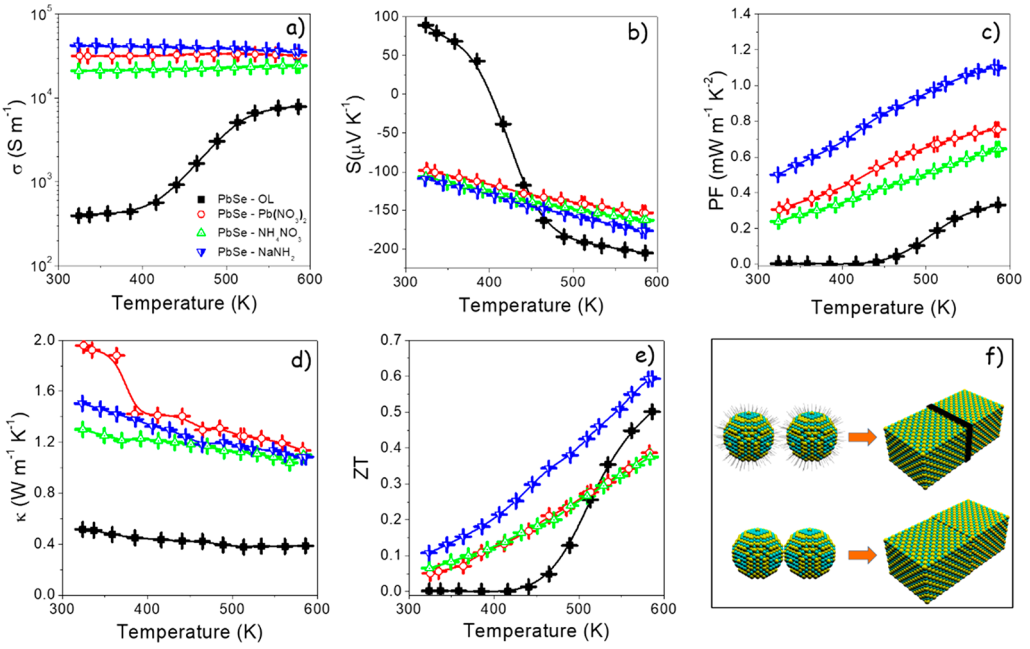

Figure 4. (a–e) Electrical conductivity, σ (a), Seebeck coefficient, S (b), power factor, PF (c), thermal conductivity, κ (d), and thermoelectric figure of merit, ZT (e) of nanocrystalline PbSe obtained from the bottom-up assembly of PbSe-OL and PbSe-LD NCs. LD was carried out using different capping agents, as labeled in the first panel (a). The same color was used for all panels. (f) Scheme of the nanomaterial obtained with and without ligand displacement.

in a similar temperature dependence of the transport properties. However, $NaNH_2$ was the salt resulting in a larger electrical conductivity increase, which we associated with the easy decomposition of the amide group during the NC consolidation.

We believe that the large differences in the temperature dependence of the electrical conductivity and Seebeck coefficient obtained between PbSe-OL and PbSe-LD samples were in large part related to significant variations of the charge carrier concentration. This variation of the charge carrier concentration was related to changes in the material composition associated with the different organic ligand removal strategies. Initial colloidal NCs were uncharged because OAc molecules compensated for the surface dangling bonds. The thermal decomposition of the OAc bond to Pb ions at the PbSe surface left oxygen ions behind, that compensated surface charge or trapped free charges.[29,76] We experimentally observe that the potential 10^{20}–10^{21} dangling bonds in PbSe-OL translated in just 10^{16} charge carriers, as measured by Hall. On the other hand, the stripping of the OAc molecules with $NaNH_2$ resulted in NCs with Pb-rich surfaces and an overall off-stoichiometric composition. Thus, high concentrations of free electrons were measured. The Hall charge carrier concentration at room temperature was $n_e = 2 \times 10^{19}$ cm^{-3} for PbSe-$NaNH_2$. In addition, during the thermal treatments, some amount of Se could leave the NCs, intensifying the stoichiometry unbalance. This effect may be insignificant in PbSe-OL samples, as the carbon left after the organic thermal decomposition may better protect the material from the chalcogen loss.

To further understand the electrical conductivity and Seebeck coefficient evolution with temperature, a charge transport model based on the standard Boltzmann transport equation[46] with the relaxation time approximation was used (see the Supporting

DOI: 10.1021/acsaem.9b02137
ACS Appl. Energy Mater. XXXX, XXX, XXX–XXX

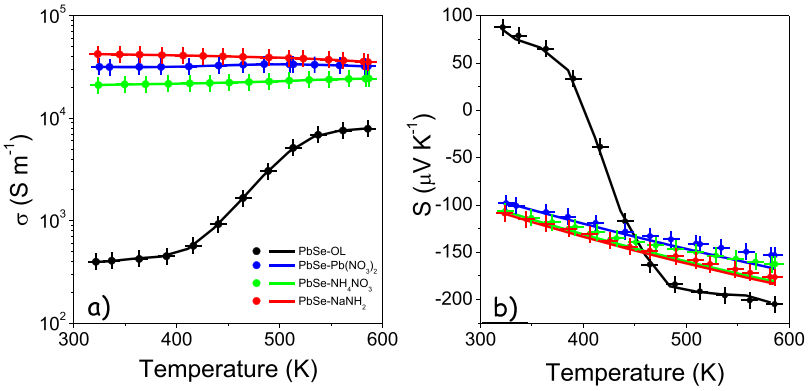

Figure 5. (a) Electrical conductivity and (b) Seebeck coefficient as a function of temperature. Symbols display the obtained experimental values, and the plotted continuous line was calculated from the two-band model.

Information). The electrical conductivity and the Seebeck coefficient of the PbSe-OL and PbSe-LD nanomaterials were fitted using this two-band model in the temperature range from 300 to 600 K. The parameters that describe the phonon scattering processes were fixed for all materials and were not allowed to change with temperature (Table S2). Using the material parameters of Table S2, it was not possible to reproduce the experimental values. Thus, we included an interface scattering as an infinite series of potential barriers to reflect the material discontinuity between NCs, reducing the electrical conductivity of the sample with respect to the bulk case. Interface scattering parameters were adjusted for each sample to simultaneously fit both electrical conductivity and Seebeck coefficient tendencies (Figure 5).

Taking into account the interface scattering, the two-band model successfully reproduced the complex temperature evolution of the electrical conductivity and Seebeck coefficient of PbSe-OL (Figure 5). The electrical conductivity increase with temperature and the complex Seebeck trend reflected an intrinsic semiconductor behavior. The sign change in the temperature evolution of the Seebeck coefficient and the different slopes of the electrical conductivity curves pointed at two different regimes in which each type of charge carrier dominated. In the low temperature region (300 K < T < 420 K), the electrical conductivity remained approximately constant and the Seebeck coefficient was positive; thus, holes dominated the charge transport in the material. In the intermediate temperature region (420 K < T < 520 K), as temperature increased, the Seebeck coefficient rapidly decreased to zero, reflecting a similar electron and hole contribution. In the highest temperature range (520 K < T < 600 K), electrons dominated the electrical conductivity, as reflected in the negative Seebeck coefficients experimentally measured.

For PbSe-OL, we used the parameters of Table S2 to describe the phonon scattering. We additionally included the interface scattering in the scattering rates of both electrons and holes. The height and the width of the barrier were used as fitting parameters, whereas the grain size was set to L = 25 nm, as we inferred from XRD measurements. The heights of the barrier for each carrier were assumed independent from each other but dependent on temperature. The initial hole concentration that best fitted the experimental results was $p = 5 \times 10^{15}$ cm^{-3}, and the best energy barrier was 0.1 eV.

On the other hand, for the PbSe-$NaNH_2$ sample, the increase of the Seebeck coefficient and the decrease of the electrical conductivity with temperature denoted that the material was completely degenerated in the whole temperature range. Thus, this trend could be well explained using only the majority carriers, electrons in this case. We assumed that the electron concentration remained constant in the whole temperature range at n = Nd (where Nd is the doping concentration with all of the impurities being ionized), while the scattering times decreased with temperature. Taking into account the Hall results, the doping concentration was set to Nd = 2×10^{19} cm^{-3}. This high charge carrier concentration was associated with a stoichiometry unbalance produced during the OAc removal and potentially from a small selenium evaporation during thermal treatments as explained above. We used the same parameters for PbSe-OL and PbSe-LD to account for the phonon scatterings. To describe the interface scattering, we used a fixed barrier width of w = 3 nm and a grain size of L = 30 nm, as given from XRD results. The barrier height was used as a fitting parameter. With the introduction of interface scattering, the experimental conductivity and Seebeck coefficients were well reproduced by the two-band model when considering a lineal temperature dependence of the chemical potential $\mu = 0.2879 + 3.4164 \times 10^{-4}T$, measured from the top of the valence band. This result was consistent with a completely degenerated semiconductor, since the chemical potential was always inside the conduction band in the whole temperature range. Concerning the interface scattering, the barrier height was temperature dependent, following a lineal trend described by $E_b = 0.26699 - 2.2495 \times 10^{-4}T$, which resulted in effective barriers slightly above those of PbSe-OL in the temperature range tested.

Figure 4d displays the thermal conductivity (κ) of the different PbSe materials in the temperature range 300−600 K. Thermal conductivities monotonically decreased with temperature for all nanomaterials. PbSe-OL was characterized by up to 3-fold lower thermal conductivities than PbSe-LD in the measured temperature range. These experimental results proved that the products from the decomposition of the OLs in the material not only blocked crystal domain growth, charge carrier transport, and possibly Se evaporation but also affected the phonon propagation. The lower thermal conductivities obtained for PbSe-OL had their origin on the carbon present in between NCs, the slightly larger interface density of PbSe-OL related with the smaller size of the crystal domains, and the higher porosity of the PbSe-OL when compared to PbSe-LD.

Finally, the TE figure of merit, ZT = $TS^2\sigma/\kappa$, increased with temperature for all materials, reaching values up to 0.5 for PbSe-OL and 0.6 for PbSe-$NaNH_2$ (Figure 4e). These values were significantly higher than those of undoped bulk PbSe and

DOI: 10.1021/acsaem.9b02137
ACS Appl. Energy Mater. XXXX, XXX, XXX−XXX

comparable with those obtained from bulk PbSe doped with Ag or Na at 600 K.[63,72] By measuring the same sample for several consecutive temperature cycles, we observed the transport properties of the PbSe nanomaterials to be stable in the measured temperature range (Figure S3).

To further demonstrate the suitability of this strategy to produce functional materials and devices, PbSe-$NaNH_2$ nanomaterials were employed to build ring-shaped TE generators.[6,77] While most of the commercially available TE devices are plate-shaped, TE devices build on a ring configuration are very convenient and appealing when heat to be harvested or delivered diffuses in a radial direction, e.g., in pipes transporting a hot fluid.[1] The assembly of several n- and p-type TE rings connected thermally in parallel and electrically in series would result in a cylindrical-tube TE generator with improved thermal contact between the hot surface and the device, maximizing the thermal power collected or delivered.

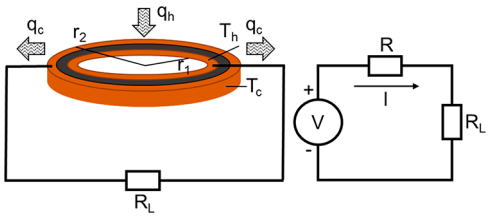

Figure 6. Basic electrical model of a ring TE generator.

In Figure 6, the basic electrical model of the ring TE generator is shown, where electrical power generated by a TE device can be generally expressed as[78]

$$P_{gen} = q_h - q_c \quad (1)$$

where q_h and q_c are the incoming and outgoing thermal power in the hot and cold side of the TE generator, respectively. Assuming mean values for S, σ, and κ, considering I as the generated electrical current that flows through the closed loop circuit, R as the electrical resistance of solely the TE material, and T_h and T_c as the temperatures in the hot and cold sides, respectively,

$$q_h = SIT_h - \frac{1}{2}I^2R + \kappa\Delta T \quad (2)$$

$$q_c = SIT_c + \frac{1}{2}I^2R + \kappa\Delta T \quad (3)$$

In the load resistance, the electrical power can be redefined as

$$P_{gen} = SI\Delta T - I^2R \quad (4)$$

Therefore, the maximum electrical power P_{max} is obtained when the load R_L has the same value as the internal resistance R

$$\frac{\partial P_{gen}}{\partial I} = 0 = S\Delta T - 2IR \rightarrow I_{max} = \frac{S\Delta T}{2R} \quad (5)$$

considering that the resistivity of a single ring is found by[79]

$$R = \frac{1}{2\pi t\sigma}\int_{r_1}^{r_2}\frac{1}{r}\,dr = \frac{1}{2\pi t\sigma}\ln\frac{r_2}{r_1} \quad (6)$$

where t is the thickness of the TE material. Then, the maximum electrical power of one TE ring generator can be expressed as a combination of material parameters:

$$P_{max} = \frac{(S\Delta T)^2}{4R} = \frac{\pi t\sigma(S\Delta T)^2}{2\ln\frac{r_2}{r_1}} \quad (7)$$

A single n-type ring, 38 mm external diameter and 29 mm internal diameter, was fabricated by filling with dried surface-engineered PbSe NCs the 1.5 mm empty space between two concentric Cu rings and hot pressing the material at 350 °C (Figure 7c). The ring was tested in a custom-made test bench. To create a radial temperature gradient, the ring was fitted between two electrically isolated metal blocks. The inner cylindrical block incorporated a heat cartridge and provided heat to the internal part of the ring. The metal block around the ring was kept at a relatively low temperature by means of commercial TE modules attached to it. The open circuit voltage was measured while heating the inner metal ring up to 530 K (Figure 7a). The measured voltage generated, around 30 mV at 190 K thermal gradient, was in good agreement with measurements of the Seebeck coefficient of the material (Figure 4b). The ring electrical resistance was measured at 1.75 mΩ, which translated into a maximum power output of around 500 mW (Figure 7b) at the maximum temperature difference reached at the test bench (190 K). Values obtained here were higher than those previously reported with a similar geometry[6] due to the larger size of the present ring, the higher Seebeck coefficient of the materials used here, and the higher temperature difference tested in the present

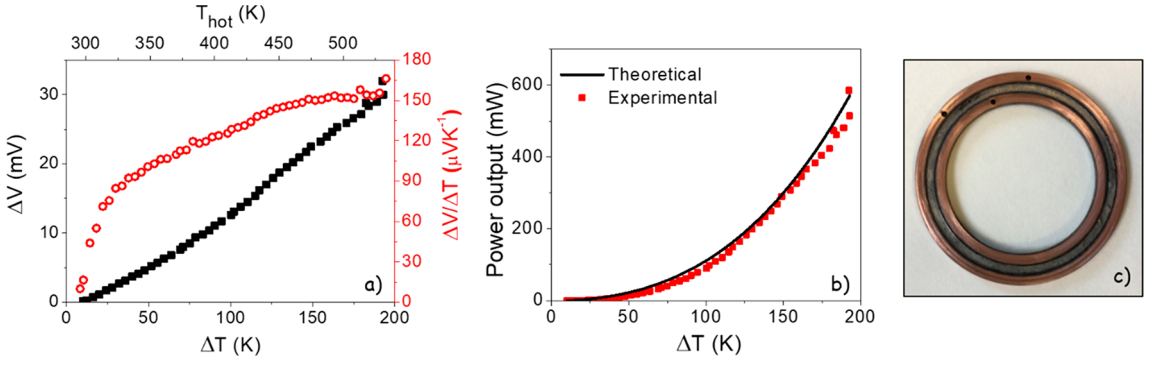

Figure 7. (a) Open circuit voltage (black squares) obtained from a single PbSe ring as a function of the temperature gradient generated by increasing the temperature at the hot side (internal part of the ring) and S (red open circles). (b) Power output of the PbSe ring as a function of the thermal gradient. Red squares represent the experimental data collection and the solid black line the theoretical calculated values taking into account experimental values for S and σ from the PbSe-LD bulk nanomaterial. (c) Image of the TE device with ring geometry.

DOI: 10.1021/acsaem.9b02137
ACS Appl. Energy Mater. XXXX, XXX, XXX−XXX

work. Experimental values were consistent with results from the electrical model, although the latter were slightly higher due to the omission of contact resistance in the model. Nevertheless, these results indicated the high potential of not only the ring configuration but also the solution-processed and bottom-up engineered TE materials and shape-adaptable devices.

4. CONCLUSIONS

In summary, PbSe nanomaterials were produced from the bottom-up assembly of PbSe colloidal NCs synthesized in the presence of OAc. The effect of two organic ligand stripping strategies was analyzed. On one hand, the organic removal by thermal decomposition resulted in a reduced crystal growth and the presence of relatively large amounts of carbon in the final material. Both lead to reduced electrical and thermal conductivities due to enhanced charge carrier and phonon scattering. Additionally, the relatively low electrical conductivities measured for PbSe nanomaterials obtained after the thermal decomposition of the organic ligands were associated with a moderate charge carrier concentration. On the other hand, the OAc displacement by metal salts had associated the introduction of a relatively large charge carrier density through the NC surface. This charge increased the interface energy barriers and the concentration of free charge carriers, resulting in a semiconductor degeneration. As a result, much higher electrical conductivities but also lower Seebeck coefficients were obtained for PbSe nanomaterials obtained from the consolidation of ligand-displaced PbSe NCs. Additionally, due to the higher density, the larger crystal domains, and the reduced phonon scattering efficiency of PbSe-LD when compared with PbSe-OL and also due to an increase of the electronic contribution, the thermal conductivity of these materials was relatively larger. Finally, a ring-shaped TE device was fabricated and tested, delivering a maximum power output of around 500 mW with 190 K temperature difference.

■ ASSOCIATED CONTENT

Supporting Information

The Supporting Information is available free of charge at https://pubs.acs.org/doi/10.1021/acsaem.9b02137.

Additional characterization data including TEM of PbSe NCs after LD and FTIR, additional TE measurements, and detailed explanation of the theoretical modeling of the material TE properties (PDF)

■ AUTHOR INFORMATION

Corresponding Authors

*E-mail: dycadavidr@unal.edu.co.

*E-mail: acabot@irec.cat.

ORCID

Doris Cadavid: 0000-0002-1376-6078

Yu Liu: 0000-0001-7313-6740

Maria Ibáñez: 0000-0001-5013-2843

Joan Daniel Prades: 0000-0001-7055-5499

Andreu Cabot: 0000-0002-7533-3251

Notes

The authors declare no competing financial interest.

■ ACKNOWLEDGMENTS

This work was supported by the Spanish Ministerio de Economía y Competitividad through the project SEHTOP (ENE2016-77798-C4-3-R) and the Generalitat de Catalunya through the project 2017SGR1246. D.C. acknowledges support from Universidad Nacional de Colombia. Y.L. acknowledges funding from the European Union's Horizon 2020 research and innovation programme under the Marie Sklodowska-Curie grant agreement no. 754411. M.I. acknowledges financial support from IST Austria.

■ REFERENCES

(1) Cadavid, D.; Ibáñez, M.; Gorsse, S.; López, A. M.; Cirera, A.; Morante, J. R.; Cabot, A. Bottom-up Processing of Thermoelectric Nanocomposites from Colloidal Nanocrystal Building Blocks: The Case of Ag2Te−PbTe. *J. Nanopart. Res.* **2012**, *14* (12), 1−10.

(2) Ibáñez, M.; Zamani, R.; Gorsse, S.; Fan, J.; Ortega, S.; Cadavid, D.; Morante, J. R.; Arbiol, J.; Cabot, A. Core−Shell Nanoparticles As Building Blocks for the Bottom-Up Production of Functional Nanocomposites: PbTe−PbS Thermoelectric Properties. *ACS Nano* **2013**, *7* (3), 2573−2586.

(3) Ortega, S.; Ibáñez, M.; Liu, Y.; Zhang, Y.; Kovalenko, M. V.; Cadavid, D.; Cabot, A. Bottom-up Engineering of Thermoelectric Nanomaterials and Devices from Solution-Processed Nanoparticle Building Blocks. *Chem. Soc. Rev.* **2017**, *46* (12), 3510−3528.

(4) Ibáñez, M.; Luo, Z.; Genç, A.; Piveteau, L.; Ortega, S.; Cadavid, D.; Dobrozhan, O.; Liu, Y.; Nachtegaal, M.; Zebarjadi, M.; et al. High-Performance Thermoelectric Nanocomposites from Nanocrystal Building Blocks. *Nat. Commun.* **2016**, *7*, 10766.

(5) Liu, Y.; Cadavid, D.; Ibáñez, M.; Ortega, S.; Martí-Sánchez, S.; Dobrozhan, O.; Kovalenko, M. V.; Arbiol, J.; Cabot, A. Thermoelectric Properties of Semiconductor-Metal Composites Produced by Particle Blending. *APL Mater.* **2016**, *4* (10), 104813.

(6) Liu, Y.; García, G.; Ortega, S.; Cadavid, D.; Palacios, P.; Lu, J.; Ibáñez, M.; Xi, L.; Roo, J. D.; López, A. M.; et al. Solution-Based Synthesis and Processing of Sn- and Bi-Doped Cu3SbSe4 Nanocrystals, Nanomaterials and Ring-Shaped Thermoelectric Generators. *J. Mater. Chem. A* **2017**, *5* (6), 2592−2602.

(7) Liu, Y.; Zhang, Y.; Ortega, S.; Ibáñez, M.; Lim, K. H.; Grau-Carbonell, A.; Martí-Sánchez, S.; Ng, K. M.; Arbiol, J.; Kovalenko, M. V.; et al. Crystallographically Textured Nanomaterials Produced from the Liquid Phase Sintering of BixSb2−XTe3 Nanocrystal Building Blocks. *Nano Lett.* **2018**, *18* (4), 2557−2563.

(8) Liu, Y.; Zhang, Y.; Lim, K. H.; Ibáñez, M.; Ortega, S.; Li, M.; David, J.; Martí-Sánchez, S.; Ng, K. M.; Arbiol, J.; et al. High Thermoelectric Performance in Crystallographically Textured N-Type $Bi_2Te_{3-x}Se_x$ Produced from Asymmetric Colloidal Nanocrystals. *ACS Nano* **2018**, *12* (7), 7174−7184.

(9) Zhang, Y.; Liu, Y.; Lim, K. H.; Xing, C.; Li, M.; Zhang, T.; Tang, P.; Arbiol, J.; Llorca, J.; Ng, K. M.; et al. Tin Diselenide Molecular Precursor for Solution-Processable Thermoelectric Materials. *Angew. Chem.* **2018**, *130* (52), 17309−17314.

(10) Li, M.; Liu, Y.; Zhang, Y.; Zuo, Y.; Li, J.; Lim, K. H.; Cadavid, D.; Ng, K. M.; Cabot, A. Crystallographically Textured SnSe Nanomaterials Produced from the Liquid Phase Sintering of Nanocrystals. *Dalton Trans.* **2019**, *48* (11), 3641−3647.

(11) Lim, K. H.; Wong, K. W.; Liu, Y.; Zhang, Y.; Cadavid, D.; Cabot, A.; Ng, K. M. Critical Role of Nanoinclusions in Silver Selenide Nanocomposites as a Promising Room Temperature Thermoelectric Material. *J. Mater. Chem. C* **2019**, *7* (9), 2646−2652.

(12) Huynh, W. U.; Dittmer, J. J.; Alivisatos, A. P. Hybrid Nanorod-Polymer Solar Cells. *Science* **2002**, *295* (5564), 2425−2427.

(13) Kovalenko, M. V.; Scheele, M.; Talapin, D. V. Colloidal Nanocrystals with Molecular Metal Chalcogenide Surface Ligands. *Science* **2009**, *324* (5933), 1417−1420.

(14) Kovalenko, M. V.; Bodnarchuk, M. I.; Zaumseil, J.; Lee, J.-S.; Talapin, D. V. Expanding the Chemical Versatility of Colloidal Nanocrystals Capped with Molecular Metal Chalcogenide Ligands. *J. Am. Chem. Soc.* **2010**, *132* (29), 10085−10092.

(15) Kovalenko, M. V.; Spokoyny, B.; Lee, J.-S.; Scheele, M.; Weber, A.; Perera, S.; Landry, D.; Talapin, D. V. Semiconductor Nanocrystals

DOI: 10.1021/acsaem.9b02137
ACS Appl. Energy Mater. XXXX, XXX, XXX−XXX

Functionalized with Antimony Telluride Zintl Ions for Nanostructured Thermoelectrics. *J. Am. Chem. Soc.* **2010**, *132* (19), 6686−6695.
(16) Kovalenko, M. V.; Bodnarchuk, M. I.; Talapin, D. V. Nanocrystal Superlattices with Thermally Degradable Hybrid Inorganic−Organic Capping Ligands. *J. Am. Chem. Soc.* **2010**, *132* (43), 15124−15126.
(17) Ibáñez, M.; Hasler, R.; Genç, A.; Liu, Y.; Kuster, B.; Schuster, M.; Dobrozhan, O.; Cadavid, D.; Arbiol, J.; Cabot, A.; et al. Ligand-Mediated Band Engineering in Bottom-Up Assembled SnTe Nanocomposites for Thermoelectric Energy Conversion. *J. Am. Chem. Soc.* **2019**, *141* (20), 8025−8029.
(18) Dong, A.; Ye, X.; Chen, J.; Kang, Y.; Gordon, T.; Kikkawa, J. M.; Murray, C. B. A Generalized Ligand-Exchange Strategy Enabling Sequential Surface Functionalization of Colloidal Nanocrystals. *J. Am. Chem. Soc.* **2011**, *133* (4), 998−1006.
(19) Rosen, E. L.; Buonsanti, R.; Llordes, A.; Sawvel, A. M.; Milliron, D. J.; Helms, B. A. Exceptionally Mild Reactive Stripping of Native Ligands from Nanocrystal Surfaces by Using Meerwein's Salt. *Angew. Chem., Int. Ed.* **2012**, *51* (3), 684−689.
(20) Nag, A.; Kovalenko, M. V.; Lee, J.-S.; Liu, W.; Spokoyny, B.; Talapin, D. V. Metal-Free Inorganic Ligands for Colloidal Nanocrystals: S2−, HS−, Se2−, HSe−, Te2−, HTe−, TeS32−, OH−, and NH2− as Surface Ligands. *J. Am. Chem. Soc.* **2011**, *133* (27), 10612−10620.
(21) Chuang, C.-H. M.; Brown, P. R.; Bulović, V.; Bawendi, M. G. Improved Performance and Stability in Quantum Dot Solar Cells through Band Alignment Engineering. *Nat. Mater.* **2014**, *13* (8), 796−801.
(22) Fan, J. Z.; Croix, A. D. L.; Yang, Z.; Howard, E.; Quintero-Bermudez, R.; Levina, L.; Jenkinson, N. M.; Spear, N. J.; Li, Y.; Ouellette, O.; et al. Ligand Cleavage Enables Formation of 1,2-Ethanedithiol Capped Colloidal Quantum Dot Solids. *Nanoscale* **2019**, *11* (22), 10774−10781.
(23) Fafarman, A. T.; Koh, W.; Diroll, B. T.; Kim, D. K.; Ko, D.-K.; Oh, S. J.; Ye, X.; Doan-Nguyen, V.; Crump, M. R.; Reifsnyder, D. C.; et al. Thiocyanate-Capped Nanocrystal Colloids: Vibrational Reporter of Surface Chemistry and Solution-Based Route to Enhanced Coupling in Nanocrystal Solids. *J. Am. Chem. Soc.* **2011**, *133* (39), 15753−15761.
(24) Koh, W.; Saudari, S. R.; Fafarman, A. T.; Kagan, C. R.; Murray, C. B. Thiocyanate-Capped PbS Nanocubes: Ambipolar Transport Enables Quantum Dot Based Circuits on a Flexible Substrate. *Nano Lett.* **2011**, *11* (11), 4764−4767.
(25) Zhang, H.; Hu, B.; Sun, L.; Hovden, R.; Wise, F. W.; Muller, D. A.; Robinson, R. D. Surfactant Ligand Removal and Rational Fabrication of Inorganically Connected Quantum Dots. *Nano Lett.* **2011**, *11* (12), 5356−5361.
(26) Nag, A.; Chung, D. S.; Dolzhnikov, D. S.; Dimitrijevic, N. M.; Chattopadhyay, S.; Shibata, T.; Talapin, D. V. Effect of Metal Ions on Photoluminescence, Charge Transport, Magnetic and Catalytic Properties of All-Inorganic Colloidal Nanocrystals and Nanocrystal Solids. *J. Am. Chem. Soc.* **2012**, *134* (33), 13604−13615.
(27) Ibáñez, M.; Hasler, R.; Liu, Y.; Dobrozhan, O.; Nazarenko, O.; Cadavid, D.; Cabot, A.; Kovalenko, M. V. Tuning P-Type Transport in Bottom-Up-Engineered Nanocrystalline Pb Chalcogenides Using Alkali Metal Chalcogenides as Capping Ligands. *Chem. Mater.* **2017**, *29* (17), 7093−7097.
(28) Ibáñez, M.; Genç, A.; Hasler, R.; Liu, Y.; Dobrozhan, O.; Nazarenko, O.; Mata, M. de la; Arbiol, J.; Cabot, A.; Kovalenko, M. V. Tuning Transport Properties in Thermoelectric Nanocomposites through Inorganic Ligands and Heterostructured Building Blocks. *ACS Nano* **2019**, *13* (6), 6572−6580.
(29) Ibáñez, M.; Korkosz, R. J.; Luo, Z.; Riba, P.; Cadavid, D.; Ortega, S.; Cabot, A.; Kanatzidis, M. G. Electron Doping in Bottom-Up Engineered Thermoelectric Nanomaterials through HCl-Mediated Ligand Displacement. *J. Am. Chem. Soc.* **2015**, *137* (12), 4046−4049.
(30) Tang, J.; Kemp, K. W.; Hoogland, S.; Jeong, K. S.; Liu, H.; Levina, L.; Furukawa, M.; Wang, X.; Debnath, R.; Cha, D.; et al. Colloidal-Quantum-Dot Photovoltaics Using Atomic-Ligand Passivation. *Nat. Mater.* **2011**, *10* (10), 765−771.
(31) Zhitomirsky, D.; Furukawa, M.; Tang, J.; Stadler, P.; Hoogland, S.; Voznyy, O.; Liu, H.; Sargent, E. H. N-Type Colloidal-Quantum-Dot Solids for Photovoltaics. *Adv. Mater.* **2012**, *24* (46), 6181−6185.
(32) Ning, Z.; Ren, Y.; Hoogland, S.; Voznyy, O.; Levina, L.; Stadler, P.; Lan, X.; Zhitomirsky, D.; Sargent, E. H. All-Inorganic Colloidal Quantum Dot Photovoltaics Employing Solution-Phase Halide Passivation. *Adv. Mater.* **2012**, *24* (47), 6295−6299.
(33) Nag, A.; Zhang, H.; Janke, E.; Talapin, D. V. Inorganic Surface Ligands for Colloidal Nanomaterials. *Z. Phys. Chem.* **2015**, *229* (1−2), 85−107.
(34) Anderson, N. C.; Owen, J. S. Soluble, Chloride-Terminated CdSe Nanocrystals: Ligand Exchange Monitored by 1H and 31P NMR Spectroscopy. *Chem. Mater.* **2013**, *25* (1), 69−76.
(35) Jung, J.; Chang, M.; Yoon, H. Interface Engineering Strategies for Fabricating Nanocrystal-Based Organic−Inorganic Nanocomposites. *Appl. Sci.* **2018**, *8* (8), 1376.
(36) Hewavitharana, I. K.; Brock, S. L. When Ligand Exchange Leads to Ion Exchange: Nanocrystal Facets Dictate the Outcome. *ACS Nano* **2017**, *11* (11), 11217−11224.
(37) Cadavid, D.; Ibáñez, M.; Shavel, A.; Durá, O. J.; de la Torre, M. A. L.; Cabot, A. Organic Ligand Displacement by Metal Salts to Enhance Nanoparticle Functionality: Thermoelectric Properties of Ag2Te. *J. Mater. Chem. A* **2013**, *1* (15), 4864−4870.
(38) Ibáñez, M.; Cadavid, D.; Zamani, R.; García-Castelló, N.; Izquierdo-Roca, V.; Li, W.; Fairbrother, A.; Prades, J. D.; Shavel, A.; Arbiol, J.; et al. Composition Control and Thermoelectric Properties of Quaternary Chalcogenide Nanocrystals: The Case of Stannite Cu2CdSnSe4. *Chem. Mater.* **2012**, *24* (3), 562−570.
(39) Ibáñez, M.; Zamani, R.; LaLonde, A.; Cadavid, D.; Li, W.; Shavel, A.; Arbiol, J.; Morante, J. R.; Gorsse, S.; Snyder, G. J.; et al. Cu2ZnGeSe4 Nanocrystals: Synthesis and Thermoelectric Properties. *J. Am. Chem. Soc.* **2012**, *134* (9), 4060−4063.
(40) Ibáñez, M.; Zamani, R.; Li, W.; Shavel, A.; Arbiol, J.; Morante, J. R.; Cabot, A. Extending the Nanocrystal Synthesis Control to Quaternary Compositions. *Cryst. Growth Des.* **2012**, *12* (3), 1085−1090.
(41) Shavel, A.; Cadavid, D.; Ibáñez, M.; Carrete, A.; Cabot, A. Continuous Production of Cu2ZnSnS4 Nanocrystals in a Flow Reactor. *J. Am. Chem. Soc.* **2012**, *134* (3), 1438−1441.
(42) Ibáñez, M.; Zamani, R.; Li, W.; Cadavid, D.; Gorsse, S.; Katcho, N. A.; Shavel, A.; López, A. M.; Morante, J. R.; Arbiol, J. Crystallographic Control at the Nanoscale to Enhance Functionality: Polytypic Cu2GeSe3 Nanoparticles as Thermoelectric Materials. *Chem. Mater.* **2012**, *24*, 4615.
(43) Ibáñez, M.; Cadavid, D.; Tamburini, U. A.; Zamani, R.; Gorsse, S.; Li, W.; Shavel, A.; López, A. M.; Morante, J. R.; Arbiol, J. Colloidal Synthesis and Thermoelectric Properties of Cu2SnSe3 Nanocrystals. *J. Mater. Chem. A* **2013**, *1*, 1421.
(44) Martin, J.; Wang, L.; Chen, L.; Nolas, G. S. Enhanced Seebeck Coefficient through Energy-Barrier Scattering in PbTe Nanocomposites. *Phys. Rev. B: Condens. Matter Mater. Phys.* **2009**, *79* (11), 115311.
(45) Mentzel, T. S.; Porter, V. J.; Geyer, S.; MacLean, K.; Bawendi, M. G.; Kastner, M. A. Charge Transport in PbSe Nanocrystal Arrays. *Phys. Rev. B: Condens. Matter Mater. Phys.* **2008**, *77* (7), No. 075316.
(46) Ziman, J. M. *Principles of the Theory of Solids*; University Press: Cambridge, U.K., 1972.
(47) Zhao, L.-D.; Tan, G.; Hao, S.; He, J.; Pei, Y.; Chi, H.; Wang, H.; Gong, S.; Xu, H.; Dravid, V. P.; et al. Ultrahigh Power Factor and Thermoelectric Performance in Hole-Doped Single-Crystal SnSe. *Science* **2016**, *351* (6269), 141−144.
(48) Cui, H.; Liu, H.; Li, X.; Wang, J.; Han, F.; Zhang, X.; Boughton, R. I. Synthesis of Bi2Se3 Thermoelectric Nanosheets and Nanotubes through Hydrothermal Co-Reduction Method. *J. Solid State Chem.* **2004**, *177* (11), 4001−4006.
(49) Gautam, U. K.; Rajamathi, M.; Meldrum, F.; Morgan, P.; Seshadri, R. A Solvothermal Route to Capped CdSe Nanoparticles. *Chem. Commun.* **2001**, No. 7, 629−630.
(50) Qu, B.; Zhang, M.; Lei, D.; Zeng, Y.; Chen, Y.; Chen, L.; Li, Q.; Wang, Y.; Wang, T. Facile Solvothermal Synthesis of Mesoporous

DOI: 10.1021/acsaem.9b02137
ACS Appl. Energy Mater. XXXX, XXX, XXX−XXX

Cu2SnS3 Spheres and Their Application in Lithium-Ion Batteries. *Nanoscale* **2011**, *3* (9), 3646−3651.
(51) Cui, H.; Liu, H.; Wang, J.; Li, X.; Han, F.; Boughton, R. I. Sonochemical Synthesis of Bismuth Selenide Nanobelts at Room Temperature. *J. Cryst. Growth* **2004**, *271* (3), 456−461.
(52) Harpeness, R.; Palchik, O.; Gedanken, A.; Palchik, V.; Amiel, S.; Slifkin, M. A.; Weiss, A. M. Preparation and Characterization of Ag2E (E = Se, Te) Using the Sonochemically Assisted Polyol Method. *Chem. Mater.* **2002**, *14* (5), 2094−2102.
(53) Arachchige, I. U.; Brock, S. L. Sol−Gel Methods for the Assembly of Metal Chalcogenide Quantum Dots. *Acc. Chem. Res.* **2007**, *40* (9), 801−809.
(54) Min, Y.; Roh, J. W.; Yang, H.; Park, M.; Kim, S. I.; Hwang, S.; Lee, S. M.; Lee, K. H.; Jeong, U. Surfactant-Free Scalable Synthesis of Bi2Te3 and Bi2Se3 Nanoflakes and Enhanced Thermoelectric Properties of Their Nanocomposites (Adv. Mater. 10/2013). *Adv. Mater.* **2013**, *25* (10), 1424−1424.
(55) Liu, H.; Cui, H.; Han, F.; Li, X.; Wang, J.; Boughton, R. I. Growth of Bi2Se3 Nanobelts Synthesized through a Co-Reduction Method under Ultrasonic Irradiation at Room Temperature. *Cryst. Growth Des.* **2005**, *5* (5), 1711−1714.
(56) Ibáñez, M.; Guardia, P.; Shavel, A.; Cadavid, D.; Arbiol, J.; Morante, J. R.; Cabot, A. Growth Kinetics of Asymmetric Bi2S3 Nanocrystals: Size Distribution Focusing in Nanorods. *J. Phys. Chem. C* **2011**, *115* (16), 7947−7955.
(57) Parker, D.; Singh, D. J. High-Temperature Thermoelectric Performance of Heavily Doped PbSe. *Phys. Rev. B: Condens. Matter Mater. Phys.* **2010**, *82* (3), No. 035204.
(58) Zhao, L.-D.; Hao, S.; Lo, S.-H.; Wu, C.-I.; Zhou, X.; Lee, Y.; Li, H.; Biswas, K.; Hogan, T. P.; Uher, C.; et al. High Thermoelectric Performance via Hierarchical Compositionally Alloyed Nanostructures. *J. Am. Chem. Soc.* **2013**, *135* (19), 7364−7370.
(59) Zhou, C.; Lee, Y. K.; Cha, J.; Yoo, B.; Cho, S.-P.; Hyeon, T.; Chung, I. Defect Engineering for High-Performance n-Type PbSe Thermoelectrics. *J. Am. Chem. Soc.* **2018**, *140* (29), 9282−9290.
(60) Huang, Z.; Zhang, Y.; Wu, H.; Pennycook, S. J.; Zhao, L.-D. Enhancing Thermoelectric Performance of P-Type PbSe through Suppressing Electronic Thermal Transports. *ACS Appl. Energy Mater.* **2019**, *2* (11), 8236−8243.
(61) Slade, T. J.; Bailey, T. P.; Grovogui, J. A.; Hua, X.; Zhang, X.; Kuo, J. J.; Hadar, I.; Snyder, G. J.; Wolverton, C.; Dravid, V. P.; et al. High Thermoelectric Performance in PbSe−NaSbSe2 Alloys from Valence Band Convergence and Low Thermal Conductivity. *Adv. Energy Mater.* **2019**, *9* (30), 1901377.
(62) Urban, J. J.; Talapin, D. V.; Shevchenko, E. V.; Murray, C. B. Self-Assembly of PbTe Quantum Dots into Nanocrystal Superlattices and Glassy Films. *J. Am. Chem. Soc.* **2006**, *128* (10), 3248−3255.
(63) Wang, H.; Pei, Y.; LaLonde, A. D.; Snyder, G. J. Heavily Doped P-Type PbSe with High Thermoelectric Performance: An Alternative for PbTe. *Adv. Mater.* **2011**, *23* (11), 1366−1370.
(64) Ravich, Yu. I.; Efimova, B. A.; Tamarchenko, V. I. *Semiconducting Lead Chalcogenides*; Plenum: New York, 1970.
(65) Androulakis, J.; Chung, D.-Y.; Su, X.; Zhang, L.; Uher, C.; Hasapis, T. C.; Hatzikraniotis, E.; Paraskevopoulos, K. M.; Kanatzidis, M. G. High-Temperature Charge and Thermal Transport Properties of the n-Type Thermoelectric Material PbSe. *Phys. Rev. B: Condens. Matter Mater. Phys.* **2011**, *84* (15), 155207.
(66) Scheele, M.; Oeschler, N.; Veremchuk, I.; Peters, S.-O.; Littig, A.; Kornowski, A.; Klinke, C.; Weller, H. Thermoelectric Properties of Lead Chalcogenide Core−Shell Nanostructures. *ACS Nano* **2011**, *5* (11), 8541−8551.
(67) Mokurala, K.; Mallick, S. Effect of Annealing Atmosphere on Quaternary Chalcogenide-Based Counter Electrodes in Dye-Sensitized Solar Cell Performance: Synthesis of Cu2FeSnS4 and Cu2CdSnS4 Nanoparticles by Thermal Decomposition Process. *RSC Adv.* **2017**, *7* (25), 15139−15148.
(68) Bhattacharya, S.; Pal, A.; Jana, A.; Datta, J. Synthesis and Characterization of CdS Nanoparticles Decorated TiO2Matrix for an Efficient N3 Based Dye Sensitized Solar Cell (DSSC). *J. Mater. Sci.: Mater. Electron.* **2016**, *27* (12), 12438−12445.
(69) Mori, T. Novel Principles and Nanostructuring Methods for Enhanced Thermoelectrics. *Small* **2017**, *13* (45), 1702013.
(70) Zheng, X.; Hou, Y.; Sun, H.-T.; Mohammed, O. F.; Sargent, E. H.; Bakr, O. M. Reducing Defects in Halide Perovskite Nanocrystals for Light-Emitting Applications. *J. Phys. Chem. Lett.* **2019**, *10* (10), 2629−2640.
(71) Carey, G. H.; Abdelhady, A. L.; Ning, Z.; Thon, S. M.; Bakr, O. M.; Sargent, E. H. Colloidal Quantum Dot Solar Cells. *Chem. Rev.* **2015**, *115* (23), 12732−12763.
(72) Wang, S.; Zheng, G.; Luo, T.; She, X.; Li, H.; Tang, X. Exploring the Doping Effects of Ag in P-Type PbSe Compounds with Enhanced Thermoelectric Performance. *J. Phys. D: Appl. Phys.* **2011**, *44* (47), 475304.
(73) Zhang, Q.; Wang, H.; Liu, W.; Wang, H.; Yu, B.; Zhang, Q.; Tian, Z.; Ni, G.; Lee, S.; Esfarjani, K.; et al. Enhancement of Thermoelectric Figure-of-Merit by Resonant States of Aluminium Doping in Lead Selenide. *Energy Environ. Sci.* **2012**, *5* (1), 5246−5251.
(74) Shanker, G. S.; Swarnkar, A.; Chatterjee, A.; Chakraborty, S.; Phukan, M.; Parveen, N.; Biswas, K.; Nag, A. Electronic Grade and Flexible Semiconductor Film Employing Oriented Attachment of Colloidal Ligand-Free PbS and PbSe Nanocrystals at Room Temperature. *Nanoscale* **2015**, *7* (20), 9204−9214.
(75) Jin, R.; Chen, G.; Pei, J.; Sun, J.; Wang, Q. Controllable Synthesis and Thermoelectric Transport Properties of Binary-Phased PbTe/PbSe Nanocrystals. *CrystEngComm* **2012**, *14* (13), 4461−4466.
(76) Marks, B. M.; Howard, H. C. The Catalytic Decomposition of Oleic Acid. *J. Phys. Chem.* **1928**, *32* (7), 1040−1048.
(77) Rowe, D. M. *Thermoelectrics Handbook: Macro to Nano*; CRC Press INC: 2006.
(78) Goupil, C.; Seifert, W.; Zabrocki, K.; Müller, E.; Snyder, G. J. Thermodynamics of Thermoelectric Phenomena and Applications. *Entropy* **2011**, *13* (8), 1481−1517.
(79) Min, G.; Rowe, D. M. Ring-Structured Thermoelectric Module. *Semicond. Sci. Technol.* **2007**, *22* (8), 880−883.

DOI: 10.1021/acsaem.9b02137
ACS Appl. Energy Mater. XXXX, XXX, XXX−XXX